Instability-Triggered Triply Negative Mechanical Metamaterial

Zian Jia and Lifeng Wang*

Department of Mechanical Engineering, State University of New York at Stony Brook, Stony Brook, New York 11794, USA

(Received 21 March 2019; revised manuscript received 11 June 2019; published 20 August 2019)

We report a three-dimensional instability-triggered mechanical metamaterial that simultaneously possesses negative stiffness, negative bulk modulus, and negative Poisson's ratio. This metamaterial is a periodic arrangement of binder-shell elements. Combining numerical simulation and micromechanics analysis, we show that the thin spherical shells dent inward under compression, which contributes to a negative Poisson's ratio. Snap-through instability is predicted by the Riks method-based simulation, revealing that the metamaterial exhibits negative incremental stiffness. Negative bulk modulus is an outcome of negative stiffness and negative Poisson's ratio. Interestingly, both incremental stiffness and incremental Poisson's ratio approach negative infinity under displacement-controlled loading when snap back takes place. We further show that a triply negative metamaterial can satisfy the strong ellipticity condition, providing a mechanism to prevent the formation of localized deformation bands even when material softening takes place. The proposed triply negative metamaterial can also serve as structural elements for applications such as extreme damping composites, extreme stiff composites, and mechanical actuators.

DOI: 10.1103/PhysRevApplied.12.024040

I. INTRODUCTION

Young's modulus (E), shear modulus (G), bulk modulus (K), and Poisson's ratio (ν) are fundamental material parameters that characterize a material's mechanical performance. Conventional materials have positive material parameters while materials with negative parameters are known as metamaterials [1–8]. A material with a negative Poisson's ratio (auxetic material) contracts laterally when compressed [4,9,10], while a material with negative stiffness deforms in the direction opposite to the applied force [3,11].

Negative material indices are of great interest not only for their rich physics, but also for their alternative applications and exceptional mechanical performances. For instance, auxetic materials can produce composites with unbounded shear to bulk modulus [12] and high crashworthiness [13,14]. Negative stiffness materials, on the other hand, can provide high energy absorption [15] and produce composites with unbounded damping as well as unbounded stiffness [3,16,17]. In recent decades, negative Poisson's ratio has been demonstrated in many material structures [10,18–20]. Negative stiffness, by contrast, is acknowledged in material softening [21], resonant systems [22,23], ferroelastic materials [24], and prestressed buckling [25]. Despite these advances, designing multiple negative metamaterials and making a negative stiffness material stable are still challenging.

Physically, unconstrained materials (with stress boundary conditions) are stable if their strain energies are positive and definite, which entails positive E, G, and K, bounding the Poisson's ratio to $-1 < \nu < 0.5$ for isotropic materials [3,26]. For cubic materials, the positive energy condition bounds the Poisson's ratio to $\nu < 0.5$ (Appendix A). Constrained materials (surface displacement boundary condition), however, have a looser stability condition, which requires the material's elasticity tensor to be strongly elliptic, such that deformations are not localized [3,12,27]. For isotropic materials, the strong ellipticity condition requires $E(1-\nu)/[(1+\nu)(1-2\nu)] > 0$ and $G > 0$ [12]. In the case of $E < 0$, it entails $\nu < -1$, implying that for conventional isotropic materials with $-1 < \nu < 0.5$, the strong ellipticity condition is not satisfied if the stiffness becomes negative. Therefore, material softening in conventional materials leads to deformation localization.

It is broadly acknowledged that deformation localization causes material failure. Examples include the shear bands in plastic materials [28–31], the collapse bands in cellular materials [32,33], and the kink bands in fiber-reinforced composites [34,35]. While introducing hardening mechanisms such as grain boundaries and precipitates features provide one applicable approach to prevent deformation localization [36], how to deal with material softening is still worth investigation. Moreover, because stable

*lifeng.wang@stonybrook.edu

homogeneous negative stiffness materials are not available, lumped negative stiffness elements must be used to design high damping composites [3,16]. Therefore, how to avoid the loss of ellipticity when negative stiffness persists is a fundamental question both in preventing deformation localization and in realistic applications of negative stiffness materials.

The conditions $E<0$ and $\nu<-1$ are necessary to develop stable negative stiffness materials, which requires the development of multiple negative metamaterials. Recently, a two-dimensional (2D) metamaterial was demonstrated to have $E<0$ and $\nu<-1$ [37]. In this study, we further develop a three-dimensional (3D) metamaterial that satisfies these conditions. In addition, the stability analysis also suggests that there is no lower bound of E and ν under displacement-controlled loading. Thus, whether a mechanism exists that can enable E and ν to approach negative infinity is another intriguing question.

Here, we develop a 3D metamaterial with triply negative material indices by harnessing the snap-through instability. Combining numerical simulations with theoretical analysis, the mechanism of triply negative material indices is explored. Moreover, the anisotropic properties of a cubic material are discussed with a focus on the strong ellipticity condition. Finally, potential applications of the triply negative metamaterials are also highlighted.

II. DESIGN OF A METAMATERIAL WITH MULTIPLE NEGATIVE INDICES

The concept of the proposed triply negative metamaterial can be illustrated on a simplified "truss" network as shown in Fig. 1(a). It has been demonstrated that if each "truss element" possesses a large tangential-to-normal stiffness ratio, the network will exhibit a negative Poisson's ratio [38]. Taken a step further, if we can bring negative stiffness to the truss elements, then the network system will exhibit negative stiffness as well as a negative bulk modulus. As such, proposing a triply negative material requires finding "truss elements" that satisfy the following conditions: 1) the element has a large tangential-to-normal stiffness ratio and 2) the element has a negative incremental (or tangent) stiffness. Note that the incremental stiffness is defined as $E^{\mathrm{inc}}=d\sigma_{11}/d\varepsilon_{11}$.

Spherical and cylindrical shells are selected as candidates for the structural elements since they can be easily dented, but are difficult to shear, satisfying the first condition. Figure 1(b) plots the deformation of several thin shell elements under compression. The two cylinders in contact element (—) and the two spherical shells in contact element (—) present positive postbuckling stiffness, violating the negative stiffness condition. The postbuckling stress rises because the contact area increases under compression, which can be tuned to decrease by introducing a binder between the spherical shells. Here, the binder

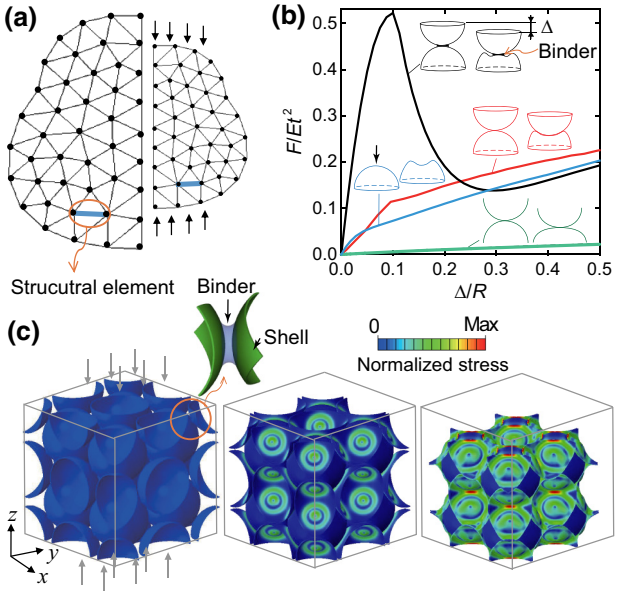

FIG. 1. The triply negative material concept. (a) A "truss" network can possess negative Poisson's ratio and negative stiffness if the structural elements possess (1) a large tangential to normal stiffness ratio and (2) a negative postbuckling stiffness. (b) Normalized force-displacement curves of different structural elements under compression (— one sphere, — two spheres in contact, — two cylinders in contact, and — two spheres connected by a binder). (c) Compression of a metamaterial produced by periodically arranging the binder-shell elements. Contour plots are shown at $\varepsilon_z=0$, -0.1, and -0.2.

is constructed by revolving arcs that tangentially connect two adjacent spherical shells, mimicking the connection of hollow sphere foam materials fabricated by sintering and selfbinding [39–41]. As depicted by — in Fig. 1(b), the binder-shell element exhibits a negative stiffness after a critical strain. Therefore, the binder-shell element satisfies both the conditions required to produce a triply negative metamaterial. Figure 1(c) demonstrates a metamaterial produced by the periodical arrangement of such binder-shell elements. The plot depicts the deformation of the metamaterial under uniaxial compression, where a negative Poisson's ratio is qualitatively observable. The existence of negative stiffness and negative bulk modulus will be presented in Sec. IV.

III. METHODS

A. Numerical simulation

The geometry of the proposed metamaterial is shown in Fig. 2. The numerical simulations are conducted on unit cells with periodic boundary conditions [42,43] utilizing finite element code ABAQUS [Fig. 2(b)]. A periodic material subjected to a macroscopic deformation gradient **F**

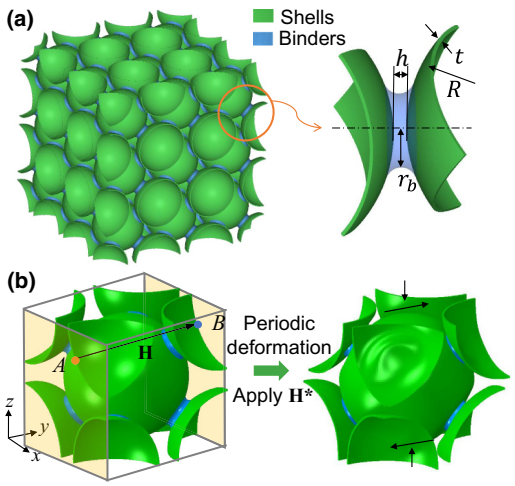

FIG. 2. (a) Geometry of the periodic 3D metamaterial. (b) The unit cell and the applied periodic boundary condition. The left shows the periodic constraints (defined by **H**) applied on a pair of points on the boundary. The right demonstrates a periodic deformation with $H^*_{33} = -0.1$ and $H^*_{23} = 0.1$.

should satisfy the following equation [42]

$$\mathbf{u}(B)-\mathbf{u}(A) = (\mathbf{F}-\mathbf{I})\{\mathbf{X}(B)-\mathbf{X}(A)\} = \mathbf{H}\{\mathbf{X}(B)-\mathbf{X}(A)\}, \quad (1)$$

where A and B are a pair of points located on the periodic boundaries. **u** denotes displacement, **X** denotes position in the reference configuration, and $\mathbf{H} = \mathbf{F}–\mathbf{I}$ is the macroscopic displacement gradient tensor. In the finite element implementation, Eq. (1) is implemented by equation constraints in ABAQUS and **H** is assigned by the displacement components of three reference nodes. For instance, the uniaxial compression in the [100] direction is applied by assigning $H_{11} = \varepsilon_{11}$, and the transverse strains are calculated from the resultant components H_{22} and H_{33}. The macroscopic first Piola-Kirchhoff stress tensor is further extracted through a virtual work consideration [42]. Note that the snap-through and snap-back buckling behaviors of the metamaterial are captured using the Riks method [44]. Moreover, the metamaterial presents a snap-through type instability, thus the introduction of structural imperfection is not necessary.

In the simulation, the binders are discretized by the *C*3*D*8 elements, while the shells are discretized using shell elements *S*3 and *S*4. The *offset command is used to offset the midplane of the shell elements such that the outer surface of the spherical shell connects to the binder. The accuracy of the mesh is ascertained through a mesh refinement study. Parametric analysis is carried out by varying relative shell thickness t/R, relative binder radius r_b/R, and stiffness ratio E_b/E_s (h/R is fixed at 0.02). The definitions of t, h, R and r_b are shown in Fig. 2, with subscripts "b" and "s" referring to the binder and shell, respectively. Here, linear elastic materials are assumed for simplicity to demonstrate the metamaterial concept.

B. The strong ellipticity condition for cubic materials

The proposed metamaterial is cubic symmetric. An unconstrained cubic material is stable if $E > 0$, $G > 0$, $K > 0$, and $\nu < 0.5$ (Appendix A). By contrast, to ensure that a material is stable under displacement constraint, the strong ellipticity condition must be satisfied [3]. The strong elliptic condition poses the following requirement on the elastic tensor, that is, $C_{ijkl}\mathbf{n}_i\mathbf{n}_j\mathbf{m}_k\mathbf{m}_l > 0$, where $\mathbf{n}_i$ and $\mathbf{m}_i$ are arbitrary unit vectors [45,46]. The physical meaning of the strong ellipticity condition is that the material should have real wave speeds in all directions to propagate the deformation to the whole material. For a cubic material, the condition of strong ellipticity can be derived based on the Hadamard inequality [47], which entails

$$C_{11} > 0,\ C_{44} > 0,\ C_{11} > C_{12}, \quad (2)$$

$$\eta \equiv C_{11} + C_{12} + 2C_{44} > 0, \quad (3)$$

$$\text{and } |C_{44} + C_{12}| < C_{44} + \sqrt{C_{11}(C_{11} + \eta/2 - |C_{11} - \eta/2|)/2}, \quad (4)$$

where C_{ij} is the elastic tensor in the Voigt notation. In the case of negative stiffness, Eqs. (2) and (3) are equivalent to the following inequalities

$$E < 0, \nu < -1, G > 0. \quad (5)$$

Note that the requirements of Eq. (5) are the same as that for isotropic materials. The additional requirement, Eq. (4), arises because of the direction-dependent material property. Equations (4) and (5) can be used as the analytical criteria to judge whether a cubic metamaterial satisfies the strong ellipticity condition. For completeness, the validation of strong ellipticity for a general anisotropic material is provided in the Appendix A.

C. Direction dependency of the material property

The proposed metamaterial is a 3D cubic material whose material properties are direction dependent. Specifically, Young's modulus depends on the direction of loading, while Poisson's ratio and shear modulus depend on both the direction of loading and the direction of measurement. For instance, Poisson's ratio (ν_{ij}) depends on the loading direction i and the lateral direction of measurement j. To visualize the direction dependency of anisotropic materials, we first calculate the compliance matrix ($\mathbf{S}_{ij}$) in a reference coordinate system. The new compliance matrix, $\mathbf{S}'_{ij}$, in an arbitrary coordinate system can be subsequently evaluated by coordinate transformation [48,49]. The new coordinate system is related to the reference system defined by Miller indices [hkl] and the angle of rotation θ. The new

compliant matrix in an arbitrary coordinate system defined by $[hkl]$ and θ has the following form (Appendix B)

$$\mathbf{S}'_{ij} = \mathbf{S}_{ij} + AF_{ij}([hkl], \theta), \tag{6}$$

where $A = (S_{11} - S_{12} - S_{44}/2)$ and expressions of F_{ij} are explicit functions. Using the new compliance matrix ($\mathbf{S}'_{ij}$), the corresponding elastic parameters in the new coordinate system can be evaluated accordingly. For example, Poisson's ratio in the new coordinate system can be evaluated as $\nu_{[hkl],\theta} = -S'_{12}/S'_{11}$. Note that Poisson's ratio depends on both $[hkl]$ and θ, therefore, a stereographic projection [50] is adapted to present the Poisson's ratio as depicted in Fig. 10.

IV. RESULTS AND DISCUSSION

Figure 3 summarizes the equilibrium paths of the proposed metamaterial with varying t/R, while all other parameters are fixed ($h/R = 0.02$, $E_b/E_s = 0.04$, $r_b/R = 0.2$). As expected, the proposed material inherits its negative incremental stiffness from the structural element. Poisson's ratio ν_{12} is within 0.05% difference of ν_{13} because of the cubic symmetry, which is consistent with the symmetric stress contours pictured in Fig. 3(b). Interestingly, we find snap back in the equilibrium path for the metamaterial with $t/R = 0.035$. Note that when snap back takes place in the equilibrium path, the actual stress-strain curve under force-controlled loading will follow the path marked by the horizontal dashed arrow in Fig. 3(a). By contrast, the path under displacement-controlled loading will follow the vertical dashed arrow, in which case the force drops abruptly from point B to point C under displacement-controlled loading, indicating an incremental stiffness of negative infinity. Similarly, a sudden drop of Poisson's ratio can also be obtained under displacement-controlled loading, corresponding to an incremental Poisson's ratio of negative infinity. Such a sudden decrease of force and Poisson's ratio corresponds to the break of deformation symmetry induced by the snap-through instability, as depicted in the bottom right of Fig. 3. Figures 3(c) and 3(d) further plot more results of t/R in the range of 0.03–0.04 to show the transition. Simulations show that snap back only takes place for $t/R = 0.34$ and 0.35. Near the snap back to no snap back transition point ($t/R \approx 0.32$), convergence difficulty is faced in simulation because of the bifurcation nature of the problem. Nevertheless, we observe the transition trend where as t/R gets smaller than 0.3, the metamaterial tends to deform symmetrically and exhibit no pattern transformation-induced snap back.

Note that here we demonstrate a metamaterial concept of how instability can be harnessed to achieve material indices approaching negative infinity. Yet, experimental realization of the metamaterial is challenging because the instability-triggered properties can be sensitive to manufacturing defects and boundary conditions. Thereby, finding defect robust triply negative metamaterial is an important topic for further research.

A. Negative Poisson's ratio at small deformation

To uncover the underlying mechanism of negative material indices, we start by evaluating the Poisson's ratio at small deformations. Figures 4(a) and 4(b) summarize the Poisson's ratio for varying geometric parameters, that is,

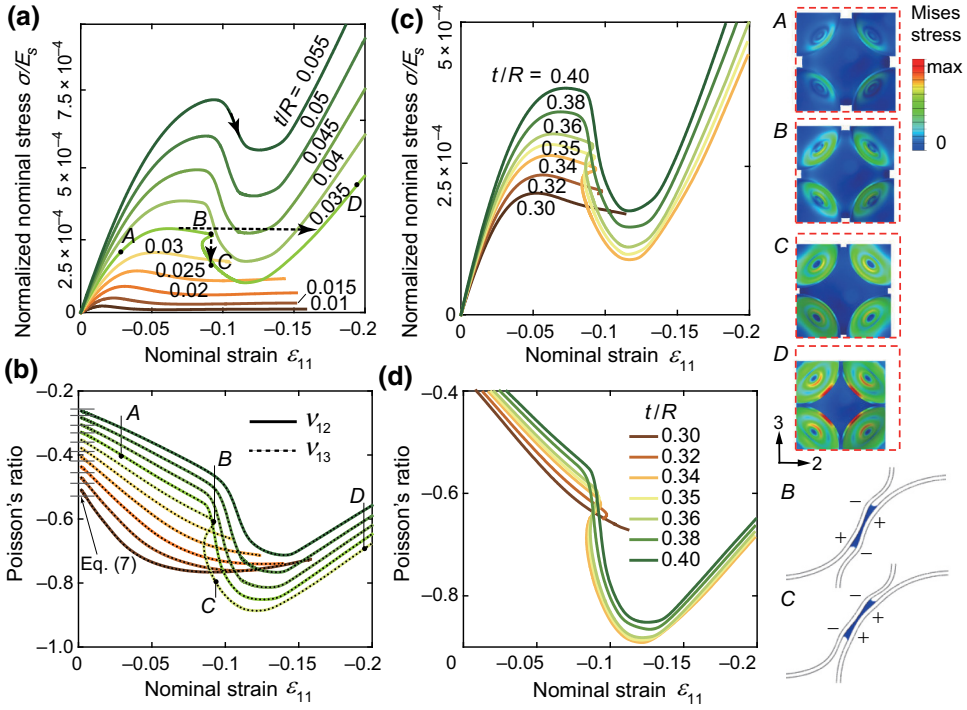

FIG. 3. (a) Normalized stress-strain curves under compression for $t/R = 0.01$–0.055. The vertical and horizontal dashed arrows highlight the path under displacement control and load control, respectively. (b) Evolution of the Poisson's ratio as a function of nominal strain for $t/R = 0.01$–0.055. Evolution of (c) stress-strain curves of the (d) Poisson's ratio for $t/R = 0.03$–0.04. Here, $r_b/R = 0.2$, $E_b/E_s = 0.04$, and $h/R = 0.02$. The stress contours at points A-D are shown in the upper right. The bottom right shows the symmetric to asymmetric pattern transformation, "+" and "−" mark the rises and dents of the shells.

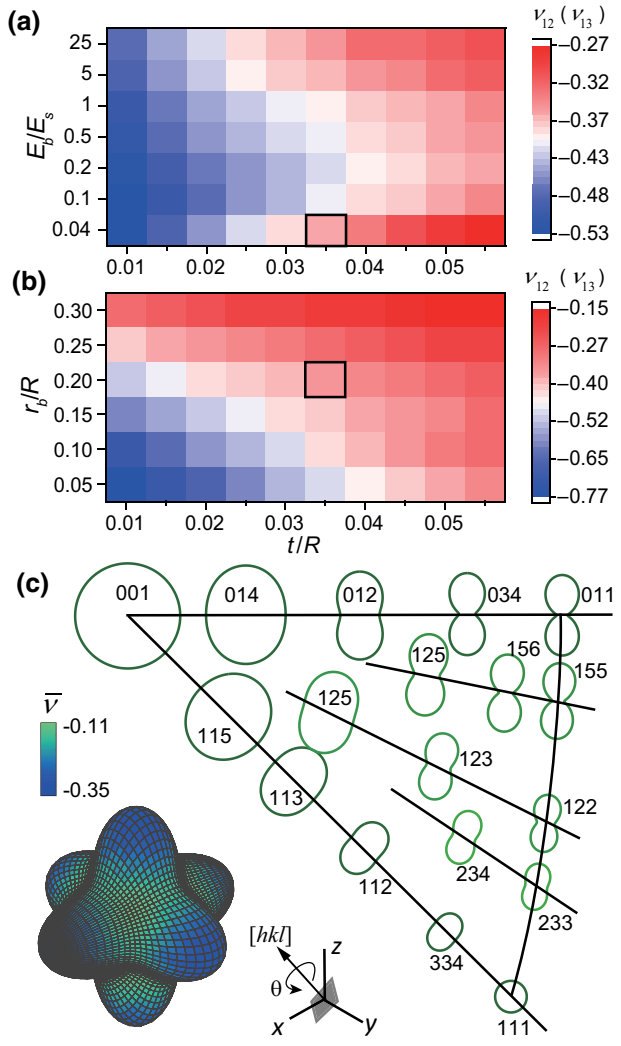

FIG. 4. Results of Poisson's ratio at small deformations. (a),(b) Poisson's ratio in the design space of $E_b/E_s = 0.04$–25, $r_b/R = 0.05$–0.3, and $t/R = 0.01$–0.055. (c) The Poisson's ratios in different loading directions [*hkl*] are superimposed on the standard triangle of the stereographic projection. The graph presents results for the metamaterial marked by black rectangles in (a),(b). The locus at [001] has a radius of $-\nu_{12} = 0.353$. All other polar plots are drawn to scale.

$t/R = 0.01$–0.055, $r_b/R = 0.05$–0.3, and $E_b/E_s = 0.04$–25. The Poisson's ratio in this design space is in the range of -0.27 to -0.77. Based on a micromechanics analysis as shown in Appendix C, the Poisson's ratio is found to be a function of the tangential to normal stiffness ratio (λ) of the structure element

$$\nu_{12} = (1 - \lambda)/(2 + \lambda). \tag{7}$$

Equation (7) suggests that Poisson's ratio becomes negative for $\lambda > 1$, providing a guideline for the design of a negative Poisson's ratio material. Results of Eq. (7) are plotted as horizontal lines in Fig. 3(b), which are consistent with the numerical results.

Furthermore, our finite element method (FEM) simulation results suggest that the normalized effective stiffness of the metamaterial scales linearly with t/R and r_b/R (for $r_b/R > 0.1$) by equation

$$E/E_s = C_1 t/R(r_b/R + C_2), \tag{8}$$

where the two parameters can be evaluated by fitting the numerical results, which gives $C_1 = 1.08$ and $C_2 = 0.0167$. A comparison of the fitting results and the direct numerical simulation results is provided in Fig. 5, showing great agreement. Note that the linear scaling relationship is advantageous for developing materials with high specific stiffness [51].

Using Eqs. (7) and (8), the geometries of the metamaterial can be tailored to achieve the desired Young's modulus and Poisson's ratio, which is an advantage of a periodic architected material. However, Eqs. (7) and (8) only present the material's behavior when loaded in the [100] direction. To further obtain the material behavior in arbitrary loading directions, simple shear simulations are first performed to evaluated G. Then, E, ν, and G in an arbitrary direction of loading can be obtained using the method described in Sec. III C. Note that Poisson's ratio ($\nu_{[hkl],\theta}$) depends on both [*hkl*] and θ, which is visualized in a stereographic projection [Fig. 4(c)]. This plot depicts the direction dependency of $\nu_{[hkl],\theta}$ for the metamaterial with $t/R = 0.035$, $r_b/R = 0.2$, and $E_b/E_s = 0.04$. It is evident from the plot that as the loading direction changes from [001] to [011], the dependency of Poisson's ratio on θ increases. For a cubic material, Poisson's ratio at an arbitrary direction of loading exhibits a two-fold symmetry except in the [100] and [111] directions. Specifically, if compressed in the [100] or [111] direction, the material will contract isotropically in all lateral directions. By contrast, the metamaterial exhibits an elliptical or peanut-shaped angle dependency of Poisson's ratio when loaded in other directions.

To give a more intuitive view, we further calculate the average Poisson's ratio ($\bar{\nu}_{[hkl]}$) in loading direction [*hkl*] by integrating over θ, which is plotted as a 3D representation surface [52] in the bottom left of Fig. 3(c). By numerically searching the solution space, we find $-0.35 < \bar{\nu} < -0.11$, suggesting that the metamaterial exhibits an omnidirectional negative Poisson's ratio. Note that not all of the proposed metamaterials possess an omnidirectional negative Poisson's ratio. Some designs only exhibit a negative Poisson's ratio in certain directions. Such direction-dependent stiffness and Poisson's ratio can enable potential applications such as direction sensitive sensors and actuators.

B. Triply negative material indices at postbuckling

Next, let us focus on the material's postbuckling behavior. To characterize the mechanical performance at relatively large deformations, the incremental stiffness

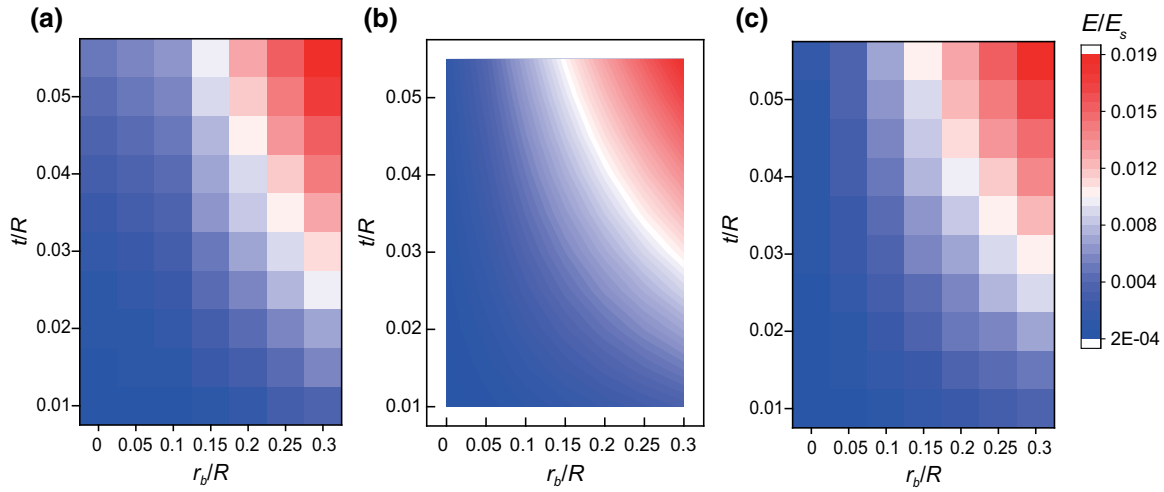

FIG. 5. Comparison of E/E_s between Eq. (8) and FEM simulations. (a) Numerical results. (b) Theoretical prediction plotted in a continuous contour and (c) theoretical prediction plotted in a Mosaic plot.

($E^{\text{inc}} = d\sigma_{11}/d\varepsilon_{11}$) and incremental Poisson's ratio ($\nu^{\text{inc}} = -d\varepsilon_{22}/d\varepsilon_{11}$) are calculated. As shown in Figs. 6(a) and 6(b), dips of E^{inc} and ν^{inc} are prominent. Interestingly, when snap back takes place ($t/R = 0.035$), both E^{inc} and ν^{inc} show singularity approaching negative infinity. To uncover the mechanism of the "anomalous" decrease of E^{inc} and ν^{inc}, the evolution of transverse strains and the deformations of adjacent sphere pairs are plotted in Figs. 6(c) and 6(d), respectively. For $t/R = 0.035$, Fig. 6(c) shows that when ε_{11} reaches a critical strain, an infinite small decrease of ε_{11} will lead to a finite reduction of both stress and transverse strain. Therefore, the incremental parameters E^{inc} and ν^{inc} approach negative infinity. The deformation fields also suggest that snap back is accompanied by a change of the material's deformation pattern.

To verify that the observed anomalies are caused by pattern transformation of the spherical shells, we compare two metamaterials with ($t/R = 0.04$) and without ($t/R = 0.03$) pattern transformation. Numerical results show that for $t/R = 0.03$, the two adjacent spheres maintain a consistent symmetric deformation pattern (Fig. 7). As such, both E^{inc} and ν^{inc} vary smoothly, exhibiting no anomalies. In

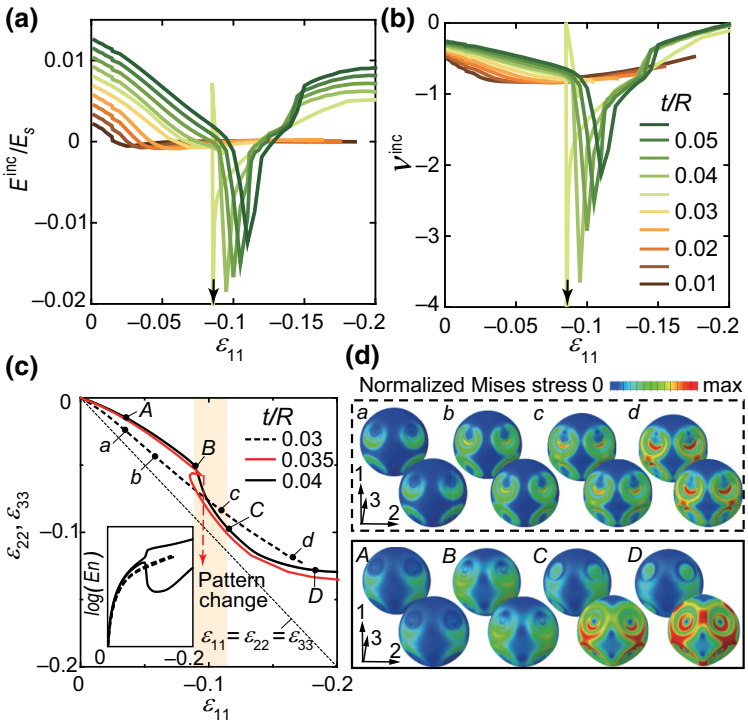

FIG. 6. (a) Incremental stiffness and (b) incremental Poisson's ratio. A singularity emerges when snap back is observed in the equilibrium path. The arrows highlight the singularity approaching negative infinity. (c) Evolution of transverse strains versus applied strains. The shaded area highlights the region of negative incremental stiffness for $t/R = 0.04$. Inset shows the evolution of strain energy (En) of two adjacent spheres. (d) The deformations of adjacent spherical shells for points (a)–(d) and (A)–(D).

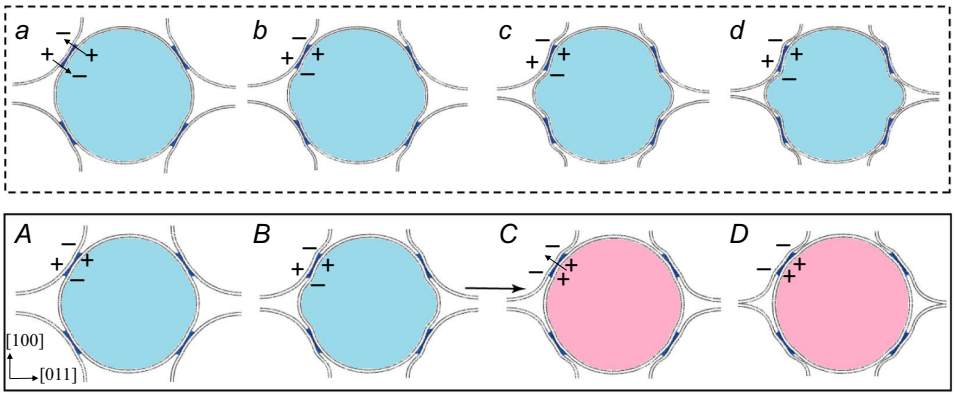

FIG. 7. (*a*)–(*d*) and (*A*)–(*D*) plot the deformation on the (011) plane for the deformation paths in Fig. 6(c). The compression is applied in the [100] direction. The "+" and "−" signs highlight the rise and dents of the spherical shells. The blue color highlights the antisymmetric deformation, while the pink color highlights the nonsymmetric deformation.

contrast, for $t/R = 0.04$, the deformation of the adjacent spheres changes from a symmetric pattern to a nonsymmetric pattern, as presented in Fig. 7. The pattern transformation takes place between point B and point C as highlighted by the shaded area in Fig. 6(c). This range is consistent with the range of negative incremental stiffness as well as a fast decrease of transverse strain ε_{22} and ε_{33}. To obtain a quantitative understanding of the pattern transformation, we further plot the strain energy evolutions of two adjacent spheres in the inset of Fig. 4(c). The plot shows that the strain energy bifurcates when pattern transformation is initiated. These results give strong evidence that the anomalies in E^{inc} and ν^{inc} result from the break of deformation symmetry, which causes an abrupt stress drop and an abrupt lateral contraction.

Note that bulk modulus can be calculated by $K = E/3(1-2\nu)$. Therefore, the proposed metamaterial with negative E and ν also leads to a negative bulk modulus. Materials with negative bulk modulus are known as negative compressive metamaterials, which have potential applications such as actuators, force amplifiers, and micromechanical controls [53]. Combing the results in this section, the proposed metamaterial can exhibit triply negative material indices by harnessing postbuckling deformation.

C. Validating the pattern transformation

So far, the numerical simulations are based on unit cells. It is acknowledged that when pattern transformation is triggered, the microscopic bifurcation could have a longer periodic length than the unit cell. Moreover, the negative stiffness $E^{\text{inc}} < 0$ and negative Poisson's ratio $\nu^{\text{inc}} < -1$ appear in the postbuckling region with strong nonlinearity. Whether or not the pattern transformation is a result of easy deformation modes should be considered. To verify that the snap-through-induced deformation mode is nontrivial and the unit cell captures the microscopic instability correctly, we further create super cells with $2\times2\times2$, $1\times1\times4$, $2\times2\times4$, $2\times2\times8$, and $3\times3\times3$ conventional unit cells. Figure 8 summarizes the postbucking deformation of different super unit cells under uniaxial compression. Results show that all the unit cells with different sizes present the same pattern transformation, verifying that the symmetric to nonsymmetric pattern transformation is nontrivial and independent of the cell size [54]. Note that fabrication defects and imperfections might change the deformation mode. Therefore, experimental verification should be presented in future study.

D. A triply negative material satisfying the strong ellipticity

As discussed previously, both E^{inc} and ν^{inc} approach negative infinity when pattern transformation takes place

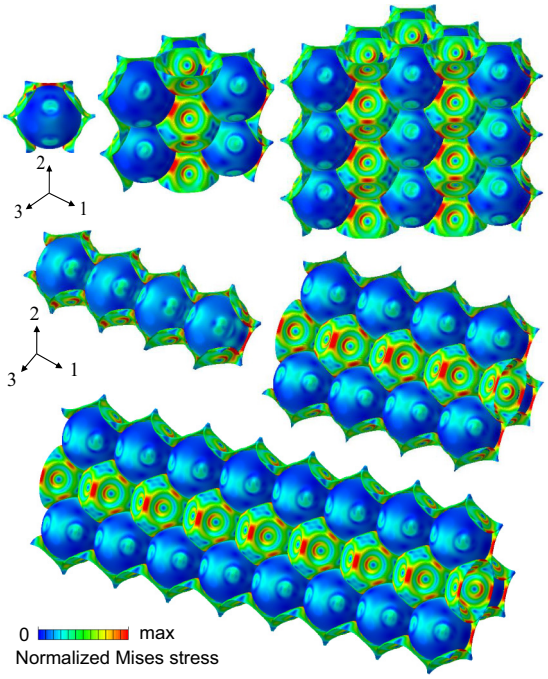

FIG. 8. Validation of the buckling pattern in multiple unit cells. The results of one conventional BCC unit cell, $2\times2\times2$, $3\times3\times3$, $1\times1\times4$, $2\times2\times4$, and $2\times2\times8$ super cells are presented at $\varepsilon_{11} = -0.15$. Part of the spheres is removed to show the deformation pattern. The results are shown for a metamaterial with $h/R = 0.02$, $E_b/E_s = 0.04$, $r_b/R = 0.2$, and $t/R = 0.04$.

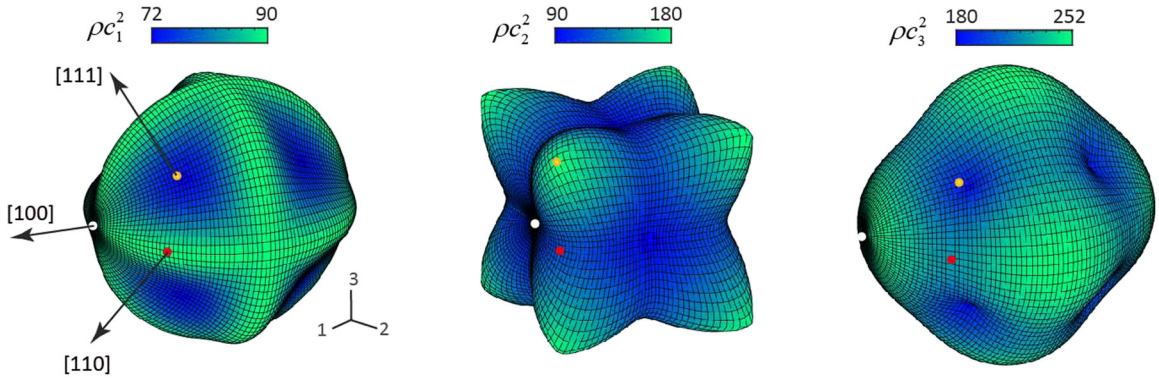

FIG. 9. The wave speeds of a metamaterial with $E^{\text{inc}} = -1194.7$ MPa, $\nu^{\text{inc}} = -3.652$, $G^{\text{inc}} = 90.04$ MPa at strain $\varepsilon_{11} = -0.095$. Results show that this metamaterial presents positive wave speeds in all directions and wave polarizations, thus satisfying the strong ellipticity condition. Note that c_1, c_2, and c_3 correspond to the minimum, secondary, and maximum wave speeds, respectively. The directions with high symmetry are also marked.

instantaneously (snap back is presented). This is a direct numerical verification to the theoretical prediction that $E \to -\infty$ and $\nu \to -\infty$ can be realized by triggering instability. In contrast, when pattern transformation takes place in a range of applied strains (other than instantaneously), finite values of $E^{\text{inc}} < 0$ and $\nu^{\text{inc}} < -1$ can be obtained. In previous studies, negative stiffness materials have a positive Poisson's ratio, which does not satisfy strong ellipticity. The proposed metamaterial here can satisfy both conditions. As an example, we evaluate the incremental parameter of a metamaterial with $r_b/R = 0.2$, $E_b/E_s = 0.04$, and $t/R = 0.04$. We find the metamaterial possesses $E^{\text{inc}}/E_s = -0.0171$, $\nu^{\text{inc}} = -3.652$, and $G^{\text{inc}}/E_s = 1.29 \times 10^{-3}$ at strain $\varepsilon_{11} = -0.095$. Using the inequalities in Eqs. (4) and (5), we find that the metamaterial satisfies the strong ellipticity condition. The wave speed in all wave propagation directions and wave polarizations are further visualized in Fig. 9.

A metamaterial with $E^{\text{inc}} < 0$ that satisfies strong ellipticity is of great application importance because it enables the use of a large block of the metamaterial (containing many unit cells) in a controllable manner. In addition, it provides a mechanism to prevent softening-induced deformation localization. Also note that the incremental stiffness and incremental Poisson's ratio become the "applicable" material parameters when prestressed to the corresponding strain. Thereby, prestressed metamaterials can be used to create composites with extremely high damping and high stiffness as reported in [3,11,16,17].

V. CONCLUSIONS

In summary, we demonstrate an instability-triggered triply negative metamaterial that is stable under displacement constraint. Without prestress (at small strains), the material exhibits negative Poisson's ratio, which can be rationally tuned by the geometric parameters. Notably, the metamaterial presents well defined direction-dependent properties, which enables potential applications like direction sensitive sensors and actuators. When prestressed to specific strain levels, the metamaterial presents simultaneous negative stiffness, negative Poisson's ratio, and negative bulk modulus. Specifically, when snap back occurs, the incremental stiffness and incremental Poisson's ratio are found to approach negative infinity under displacement-controlled loading. Importantly, although the metamaterial exhibits negative incremental stiffness, it satisfies the strong ellipticity condition. This unique property enables the application of homogeneous negative stiffness and negative compressibility materials, opening alternative possibilities to prevent deformation localization.

Moreover, recent progress in selfassembling techniques [55–57] makes the fabrication of the metamaterial at nanoscales possible, which facilitates the applications of the triply negative metamaterials in areas including lightweight armor systems, energy damping systems, and fast actuation devices. In addition, previous studies have shown that the hollow sphere foam materials possess lightweight tunable thermal conductivity, and acoustic absorption ability [41,58]. Therefore, the proposed metamaterial also serves as a promising candidate for achieving multifunctionality, which is of particular interest in space travel.

ACKNOWLEDGMENTS

The authors sincerely acknowledge Professor Roderic Lakes for his insightful comments and valuable suggestions during the course of this research. This research was partly supported by the National Science Foundation (Grant No. CMMI-1462270). The authors also acknowledge the use of the Center for Functional Nanomaterials facility at Brookhaven National Laboratory.

TABLE I. Material parameters satisfying the strong ellipticity condition for isotropic materials under displacement constraint.

Region 1, negative ν	Region 2, triply negative	Region 3, negative K
$G>0$	$G>0$	$G>0$
$E>0, -1<\nu<0.5$	$E<0, \nu<-1$	$E>0, \nu>1$
$K>0$	$-G/3<K<0$	$-4G/3<K<-G/3$

APPENDIX A: STABILITY ANALYSIS

Unconstrained materials

For unconstrained materials to be stable, the positive definite strain energy condition should be satisfied, which requires the energy densities including $E\varepsilon_{11}^2/2$, $G\gamma_{12}^2/2$ and $K\varepsilon_B^2/2$ to be positive. Thereby, E, G, and K should be positive. For isotropic materials, $G=E/2(1+\nu)$ and $K=3(1-2\nu)/E$. Thus, the positive E, G, and K requirement derives $-1<\nu<0.5$. For cubic materials, by contrast, only the equation $K=3(1-2\nu)/E$ holds. Thus, the stability condition becomes $\nu<0.5$. For general anisotropic materials whose E, G, and K are independent, no bound exists for the Poisson's ratio.

The strong ellipticity condition for constrained materials

For a material to be stable under displacement constraint, the strong ellipticity condition must be satisfied [3]. The strong elliptic condition poses the following requirement on the elastic tensor, $C_{ijkl}\mathbf{n}_i\mathbf{n}_j\mathbf{m}_k\mathbf{m}_l>0$, where $\mathbf{n}_i$ and $\mathbf{m}_i$ are arbitrary unit vectors [45,46]. An alternative form of this requirement is that the acoustic tensor $A_{ik}=C_{ijkl}\mathbf{n}_j\mathbf{n}_l$ should be positive definite for all possible $\mathbf{n}$. Here, the discussion is based on the acoustic tensor.

For an isotropic material, the three wave propagation speeds c_L^2, c_S^2, and c_S^2 are direction independent and have the following expressions [59]

$$c_L^2=\frac{E(1-\nu)}{\rho(1+\nu)(1-2\nu)},\ c_S^2=\frac{G}{\rho}, \tag{A1}$$

where the subscripts L and S indicate the longitudinal mode and shear mode, respectively. Positive definite A_{ik} thus requires $E(1-\nu)/(1+\nu)(1-2\nu)>0$ and $G>0$. Based on these inequalities, the material property space that satisfies the strong ellipticity condition can be obtained as summarized in Table I, which has three regions.

For a general anisotropic material, the elastic wave velocity is direction dependent. Note that equivalent inequality conditions have been derived mathematically, but the proposed conditions are not explicit and still require a numerical computation [47]. Alternatively, a verification of the strong ellipticity condition can be performed by checking the wave propagation speed for all incident directions and wave polarizations. This is achieved by numerically calculating the eigenvalues of the acoustic tensor, $A_{ik}=C_{ijkl}\mathbf{n}_j\mathbf{n}_l$, for varying directions of $\mathbf{n}$. $\mathbf{n}$ is the wave propagation direction defined as $\mathbf{n}=[\cos\theta\sin\varphi,\ \sin\theta\sin\varphi,\ \cos\varphi]^T$, where θ is the azimuth angle and φ is the zenith angle. The complete range of propagation directions is computed with θ varying from $-180°$ to $180°$ and φ varying from $0°$ to $180°$. Given C_{ijkl} and $\mathbf{n}$, A_{ik} can be calculated and its three eigenvalues correspond to wave propagation speeds of three wave polarizations (one quasilongitudinal and two quasishear), ρc_L^2, ρc_{S1}^2, and ρc_{S2}^2. The described procedure can be realized using a MATLAB program.

APPENDIX B: DIRECTION DEPENDENCY OF A CUBIC MATERIAL

Based on the cubic symmetry, the elastic compliant tensor S_{ijkm} of a cubic material can be written in the following form [49]

$$S'_{ijkm}=S_{12}\delta_{ij}\delta_{km}+\frac{1}{4}S_{44}(\delta_{ik}\delta_{jm}+\delta_{im}\delta_{jk})+(S_{11}-S_{12}-\frac{1}{4}S_{44})a_{it}a_{jt}a_{kt}a_{mt}, \tag{B1}$$

where S_{ijkm} denotes the compliant tensor in the original lattice structure and $'$ denotes the compliant tensor in the new coordinate system defined by $[hkl]$ and θ. The notation $a_{it}a_{jt}a_{kt}a_{mt}$ is adopted from [49], which equals $\sum_{t=1,2,3} a_{it}a_{jt}a_{kt}a_{mt}$. The transformation matrix is

$$a_{st}=\begin{bmatrix} \frac{h}{\sqrt{h^2+k^2+l^2}} & \frac{k}{\sqrt{h^2+k^2+l^2}} & \frac{l}{\sqrt{h^2+k^2+l^2}} \\ -\frac{\sqrt{k^2+l^2}\cos\theta}{\sqrt{h^2+k^2+l^2}} & \frac{hk\cos\theta}{\sqrt{k^2+l^2}\sqrt{h^2+k^2+l^2}}-\frac{l\sin\theta}{\sqrt{l^2+k^2}} & \frac{hl\cos\theta}{\sqrt{k^2+l^2}\sqrt{h^2+k^2+l^2}}+\frac{k\sin\theta}{\sqrt{l^2+k^2}} \\ \frac{\sqrt{k^2+l^2}\sin\theta}{\sqrt{h^2+k^2+l^2}} & -\frac{l\cos\theta}{\sqrt{h^2+k^2}}-\frac{hk\sin\theta}{\sqrt{k^2+l^2}\sqrt{h^2+k^2+l^2}} & \frac{k\cos\theta}{\sqrt{h^2+k^2}}-\frac{hl\sin\theta}{\sqrt{k^2+l^2}\sqrt{h^2+k^2+l^2}} \end{bmatrix}. \tag{B2}$$

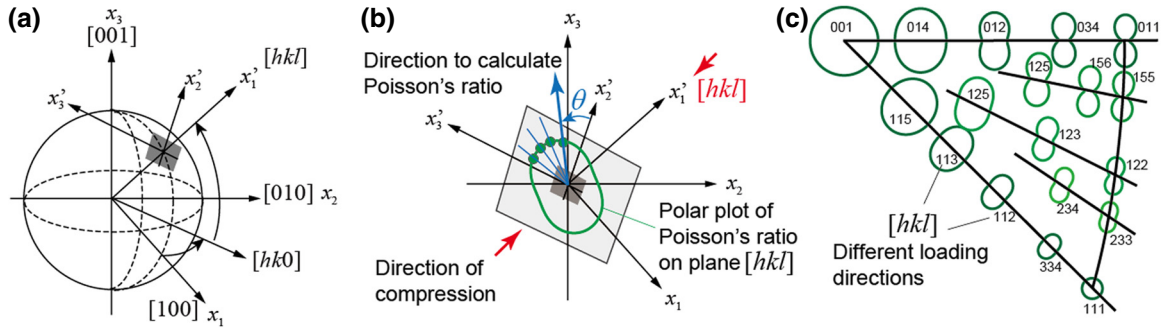

FIG. 10. Schematics illustrating the Poisson's ratio ν_{ij} of an anisotropic material on an arbitrary loading direction i and secondary direction of measurement j, which are defined by $[hkl]$ and θ, respectively. For each direction of loading, the angle dependency of Poisson's ratio is plotted on a polar plot. The stereographic projection in crystallography is further used to give a full picture of how Poisson's ratio depends on both $[hkl]$ and θ.

In order to derive the compliant matrix, a transformation between matrix notation and tensor notation should be performed first. Using $S'_{11} = S'_{1111}$, $S'_{12} = S'_{1122}$, and $S'_{44} = 4S'_{2323}$, the following equations are derived from Eq. (B1)

$$S'_{11} = S_{12} + \left(S_{11} - S_{12} - \frac{1}{2}S_{44}\right)(1 - a_{1t}a_{1t}a_{1t}a_{1t}), \tag{B3a}$$

$$S'_{12} = S_{12} + \left(S_{11} - S_{12} - \frac{1}{2}S_{44}\right)a_{1t}a_{2t}a_{1t}a_{2t}, \tag{B3b}$$

$$S'_{44} = S_{44} + 4\left(S_{11} - S_{12} - \frac{1}{2}S_{44}\right)a_{2t}a_{3t}a_{2t}a_{3t}. \tag{B3c}$$

All these equations can be written in a general form as Eq. (6) in the main text,

$$S'_{ij} = S_{ij} + AF_{ij}([hkl], \theta), \tag{B4}$$

where $A = [S_{11} - S_{12} - (1/2)S_{44}]$ is the anisotropic parameter. $F_{ij}([hkl], \theta)$ is a function of direction vector $[hkl]$ and rotation angle θ. The expression of F_{ij} is calculated by combining Eqs. (B2) and (B3), which are listed in the following

$$F_{11} = -2(h^2k^2 + k^2l^2 + l^2h^2),$$

$$F_{12} = \frac{2}{k^2 + l^2}[(k^4 + k^2l^2 + l^4)\cos^2\theta + hkl(l^2 - k^2)\cos\theta\sin\theta + k^2l^2\sin^2\theta],$$

$$F_{13} = \frac{2}{k^2 + l^2}[k^2l^2\cos^2\theta + hkl(k^2 - l^2)\cos\theta\sin\theta + h^2(k^4 + k^2l^2 + l^4)\sin^2\theta],$$

$$F_{44} = \frac{4}{(k^2 + l^2)^2}[(k^2 + l^2)^4\cos^2\theta\sin^2\theta + (l\cos\theta + hk\sin\theta)^2(hk\cos\theta - l\sin\theta)^2 + (hl\cos\theta + k\sin\theta)^2(k\cos\theta - hl\sin\theta)^2].$$

The stiffness of a cubic material in an arbitrary direction $[hkl]$ can then be calculated from

$$\frac{1}{E'} = \frac{1}{E_{[hkl]}} = S'_{11} = \frac{1}{E_{[100]}} - 2A(h^2k^2 + k^2l^2 + l^2h^2). \tag{B5}$$

Equation (B5) recovers the elastic representative surface of a cubic material as in [52]. Note that $E_{[hkl]}$ only depends on the direction of compression $[hkl]$.

Using a similar approach, Poisson's ratio can be derived as

$$\nu' = \nu_{[hkl],\theta} = -\frac{S'_{12}}{S'_{11}} = -\frac{S_{12} + AF_{12}([hkl], \theta)}{S_{11} + AF_{11}([hkl], \theta)}. \tag{B6}$$

The Poisson's ratio depends on both $[hkl]$ and θ, thus the stereographic projection in crystallography is adapted to visualize how Poisson's ratio evolves under different loading directions (Fig. 10).

In addition, the average value of ν' on the $[hkl]$ plane can be calculated by integrating over angle θ

$$\overline{S}'_{ij} = \frac{1}{2\pi}\int_0^{2\pi}\int (S_{ij} + AF_{ij}([hkl], \theta))d\theta = S_{ij} + A\frac{1}{2\pi}\int_0^{2\pi} F_{ij}([hkl], \theta)d\theta = S_{ij} + A\overline{F}_{ij}([hkl]). \tag{B7}$$

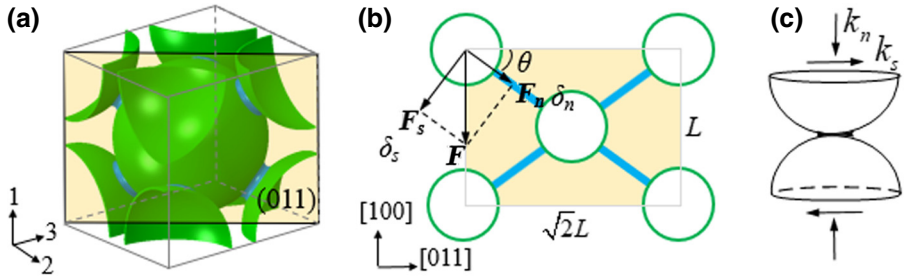

FIG. 11. (a) The light yellow color highlights the (011) plane used for micromechanics analysis. The unit cell is under uniaxial compression in direction 1. (b) **F** denotes the resultant force on each binder-shell element in direction [100]. $\mathbf{F}_n$ and $\mathbf{F}_t$ denote the force components in the normal and tangent directions and δ_n and δ_t denote the corresponding displacements. The spheres and binders are not drawn to scale for easy viewing. (c) Definition of the normal and tangential stiffness of the binder-shell structural element.

The averages of F_{ij} are given in the following

$$\overline{F}_{11} = F_{11}, \tag{B8}$$

$$\bar{F}_{12} = \frac{1}{k^2+l^2}[k^2l^2 + h^2(k^4 + k^2l^2 + l^4)], \tag{B9}$$

$$\bar{F}_{13} = \frac{1}{k^2+l^2}[k^2l^2 + h^2(k^4 + k^2l^2 + l^4)], \tag{B10}$$

$$\bar{F}_{44} = \frac{1}{2(k^2+l^2)^2}[(k^2+l^2)^4 + (h^2k^2+l^2)^2 + (k^2+h^2l^2)^2]. \tag{B11}$$

An elastic representative surface of the average Poisson's ratio, $\bar{\nu}'$, is plotted in Fig. 4(c).

APPENDIX C: MICROMECHANICS ANALYSIS

In order to derive a theoretical prediction of Poisson's ratio at small deformation, we perform a micromechanics analysis on the unit cell. The analysis is based on force equilibrium in the (100) plane (Fig. 11). Assume the force applied on each binder-shell element in the direction [100] is **F**. Denote the force components in the normal and tangent directions as $\mathbf{F}_n$ and $\mathbf{F}_t$ and the corresponding displacements as δ_n and δ_t. The normal and tangential stiffness of the structural element are k_n and k_t, which are related to the force and displacement by

$$\delta_n = F_n/K_n, \delta_t = F_t/K_t. \tag{C1}$$

The resultant displacements in the [100] and [011] directions contributed by δ_n and δ_t are

$$\delta_{[100]} = \delta_n \sin\theta + \delta_t \cos\theta, \tag{C2}$$

$$\delta_{[011]} = \delta_n \cos\theta - \delta_t \sin\theta, \tag{C3}$$

where θ is the angle shown in Fig. 11. Moreover, the displacements in the [010] and [001] directions are related to the displacement in the [011] direction by

$$\delta_{[010]} = \delta_{[001]} = \delta_{[011]}/\sqrt{2}. \tag{C4}$$

Combining Eqs. (C1)–(C4) with relations $F_n = F\sin\theta$ and $F_t = F\cos\theta$, we have

$$\nu_{12} = \frac{\delta_{[010]}}{\delta_{[100]}} = \frac{\sin\theta\cos\theta(1 - k_t/k_n)}{\sqrt{2}(\cos^2\theta + \sin^2\theta k_t/k_n)}. \tag{C5}$$

In a bcc lattice, $\sin\theta = 1/\sqrt{3}$, $\cos\theta = \sqrt{2}/\sqrt{3}$. Plugging this into Eq. (C5) and denoting k_t/k_n as λ, we derive Eq. (7) in the main text

$$\nu_{12} = \nu_{13} = \frac{1-\lambda}{2+\lambda}. \tag{C6}$$

[1] K. Bertoldi, V. Vitelli, J. Christensen, and M. van Hecke, Flexible mechanical metamaterials, Nat. Rev. Mater. **2**, natrevmats201766 (2017).

[2] X. Yu, J. Zhou, H. Liang, Z. Jiang, and L. Wu, Mechanical metamaterials associated with stiffness, rigidity and compressibility: A brief review, Prog. Mater Sci. **94**, 114 (2018).

[3] R. S. Lakes, T. Lee, A. Bersie, and Y. Wang, Extreme damping in composite materials with negative-stiffness inclusions, Nature **410**, 565 (2001).

[4] R. Lakes, Foam structures with a negative Poisson's ratio, Science **235**, 1038 (1987).

[5] C. Kane and T. Lubensky, Topological boundary modes in isostatic lattices, Nat. Phys. **10**, 39 (2014).

[6] G. Milton, *The theory of composites* (Cambridge University Press, Cambridge, 2002).

[7] R. H. Baughman, S. Stafström, C. Cui, and S. O. Dantas, Materials with negative compressibilities in one or more dimensions, Science **279**, 1522 (1998).

[8] C. Coulais, D. Sounas, and A. Alù, Static non-reciprocity in mechanical metamaterials, Nature **542**, 461 (2017).

[9] J. Cherfas, Stretching the point; new materials that get fatter-rather than thinner-when they're stretched may have some revolutionary implications, Science **247**, 630 (1990).

[10] G. W. Milton, Composite materials with Poisson's ratios close to—1, J. Mech. Phys. Solids **40**, 1105 (1992).

[11] R. Lakes and W. Drugan, Dramatically stiffer elastic composite materials due to a negative stiffness phase?, J. Mech. Phys. Solids **50**, 979 (2002).

[12] S. Xinchun and R. S. Lakes, Stability of elastic material with negative stiffness and negative Poisson's ratio, Phys. Status Solidi (b) **244**, 1008 (2007).

[13] S. Mohsenizadeh, R. Alipour, M. S. Rad, A. F. Nejad, and Z. Ahmad, Crashworthiness assessment of auxetic foam-filled tube under quasi-static axial loading, Mater. Des. **88**, 258 (2015).

[14] S. Hou, T. Li, Z. Jia, and L. Wang, Mechanical properties of sandwich composites with 3d-printed auxetic and non-auxetic lattice cores under low velocity impact, Mater. Des. **160**, 1305 (2018).

[15] S. Shan, S. H. Kang, J. R. Raney, P. Wang, L. Fang, F. Candido, J. A. Lewis, and K. Bertoldi, Multistable architected materials for trapping elastic strain energy, Adv. Mater. **27**, 4296 (2015).

[16] R. Lakes, Extreme damping in compliant composites with a negative-stiffness phase, Philos. Mag. Lett. **81**, 95 (2001).

[17] T. Jaglinski, D. Kochmann, D. Stone, and R. Lakes, Composite materials with viscoelastic stiffness greater than diamond, Science **315**, 620 (2007).

[18] R. S. Lakes, Negative-Poisson's-ratio materials: Auxetic solids, Ann. Rev. Mater. Res. **47**, 63 (2017).

[19] I. Shufrin, E. Pasternak, and A. V. Dyskin, Negative Poisson's ratio in hollow sphere materials, Int. J. Solids Struct. **54**, 192 (2015).

[20] R. H. Baughman, J. M. Shacklette, A. A. Zakhidov, and S. Stafström, Negative Poisson's ratios as a common feature of cubic metals, Nature **392**, 362 (1998).

[21] F.-K. Chang and K.-Y. Chang, A progressive damage model for laminated composites containing stress concentrations, J. Compos. Mater. **21**, 834 (1987).

[22] Z. Liu, X. Zhang, Y. Mao, Y. Zhu, Z. Yang, C. T. Chan, and P. Sheng, Locally resonant sonic materials, Science **289**, 1734 (2000).

[23] N. Fang, D. Xi, J. Xu, M. Ambati, W. Srituravanich, C. Sun, and X. Zhang, Ultrasonic metamaterials with negative modulus, Nat. Mater. **5**, 452 (2006).

[24] E. Salje, Phase transitions in ferroelastic and co-elastic crystals, Ferroelectrics **104**, 111 (1990).

[25] J. Qiu, J. H. Lang, and A. H. Slocum, A curved-beam bistable mechanism, J. Microelectromech. Syst. **13**, 137 (2004).

[26] S. P. Timoshenko and J. Goodier, *Theory of elasticity* (McGraw-Hill Publishing Company, New York, 1970).

[27] J. K. Knowles and E. Sternberg, On the failure of ellipticity and the emergence of discontinuous deformation gradients in plane finite elastostatics, J. Elastic. **8**, 329 (1978).

[28] D. Bigoni, *Nonlinear solid mechanics: bifurcation theory and material instability* (Cambridge University Press, Cambridge, 2012).

[29] R. Hill, Acceleration waves in solids, J. Mech. Phys. Solids **10**, 1 (1962).

[30] J. R. Rice, in *14th International Congress of theoretical and applied mechanics* (OSTI.gov, Netherlands, 1976).

[31] S. Harren, H. Deve, and R. Asaro, Shear band formation in plane strain compression, Acta Metall. **36**, 2435 (1988).

[32] S. D. Papka and S. Kyriakides, In-plane crushing of a polycarbonate honeycomb, Int. J. Solids Struct. **35**, 239 (1998).

[33] S. D. Papka and S. Kyriakides, Experiments and full-scale numerical simulations of in-plane crushing of a honeycomb, Acta Mater. **46**, 2765 (1998).

[34] R. Gutkin, S. Pinho, P. Robinson, and P. Curtis, On the transition from shear-driven fibre compressive failure to fibre kinking in notched CFRP laminates under longitudinal compression, Compos. Sci. Technol. **70**, 1223 (2010).

[35] M. Harraez, A. C. Bergan, C. Gonzalez, and C. S. Lopes, Modeling Fiber Kinking at the Microscale and Mesoscale (2018).

[36] M.-S. Pham, C. Liu, I. Todd, and J. Lertthanasarn, Damage-tolerant architected materials inspired by crystal microstructure, Nature **565**, 305 (2019).

[37] T. A. Hewage, K. L. Alderson, A. Alderson, and F. Scarpa, Double-negative mechanical metamaterials displaying simultaneous negative stiffness and negative Poisson's ratio properties, Adv. Mater. **28**, 10323 (2016).

[38] L. Rothenburg, A. A. Berlin, and R. J. Bathurst, Microstructure of isotropic materials with negative Poisson's ratio, Nature **354**, 470 (1991).

[39] Z. Wang, T. Zhang, B. K. Park, W. I. Lee, and D. J. Hwang, Minimal contact formation between hollow glass microparticles toward low-density and thermally insulating composite materials, J. Mater. Sci. **52**, 6726 (2017).

[40] W. Sanders and L. Gibson, Mechanics of hollow sphere foams, Mater. Sci. Eng. A **347**, 70 (2003).

[41] Z. Jia, Z. Wang, D. Hwang, and L. Wang, Prediction of the Effective Thermal Conductivity of Hollow Sphere Foams, ACS Appl. Energy Mater. **1**, 1146 (2018).

[42] M. Danielsson, D. Parks, and M. Boyce, Three-dimensional micromechanical modeling of voided polymeric materials, J. Mech. Phys. Solids **50**, 351 (2002).

[43] L. Wang, M. C. Boyce, C. Y. Wen, and E. L. Thomas, Plastic dissipation mechanisms in periodic microframe-structured polymers, Adv. Funct. Mater. **19**, 1343 (2009).

[44] E. Riks, An incremental approach to the solution of snapping and buckling problems, Int. J. Solids Struct. **15**, 529 (1979).

[45] G. Geymonat, S. Müller, and N. Triantafyllidis, Homogenization of nonlinearly elastic materials, microscopic bifurcation and macroscopic loss of rank-one convexity, Arch. Ration. Mech. Anal. **122**, 231 (1993).

[46] D. Han, H.-H. Dai, and L. Qi, Conditions for strong ellipticity of anisotropic elastic materials, J. Elastic. **97**, 1 (2009).

[47] L. Zubov and A. Rudev, Criterion for the strong ellipticity of the equations of motion of an anisotropic linear-elastic material, J. Appl. Math. Mech. **80**, 485 (2016).

[48] J. Turley and G. Sines, Anisotropic behaviour of the compliance and stiffness coefficients for cubic materials, J. Phys. D: Appl. Phys. **4**, 1731 (1971).
[49] T. Thomas, On the stress-strain relations for cubic crystals, Proc. Natl. Acad. Sci. **55**, 235 (1966).
[50] K. M. Knowles and P. R. Howie, The directional dependence of elastic stiffness and compliance shear coefficients and shear moduli in cubic materials, J. Elastic. **120**, 87 (2015).
[51] X. Zheng, Howon Lee, Todd H. Weisgraber, Maxim Shusteff, Joshua DeOtte, Eric B. Duoss, Joshua D. Kuntz, Monika M. Biener, Qi Ge, Julie A. Jackson, Sergei O. Kucheyev, Nicholas X. Fang, and Christopher M. Spadaccini, Ultralight, ultrastiff mechanical metamaterials, Science **344**, 1373 (2014).
[52] J. F. Nye, *Physical properties of crystals: their representation by tensors and matrices* (Oxford University Press, Oxford, 1985).
[53] Z. G. Nicolaou and A. E. Motter, Mechanical metamaterials with negative compressibility transitions, Nat. Mater. **11**, 608 (2012).
[54] M. Laroussi, K. Sab, and A. Alaoui, Foam mechanics: Nonlinear response of an elastic 3D-periodic microstructure, Int. J. Solids Struct. **39**, 3599 (2002).
[55] B. Hatton, L. Mishchenko, S. Davis, K. H. Sandhage, and J. Aizenberg, Assembly of large-area, highly ordered, crack-free inverse opal films, Proc. Natl. Acad. Sci. **107**, 10354 (2010).
[56] A. Dong, X. Ye, J. Chen, and C. B. Murray, Two-dimensional binary and ternary nanocrystal superlattices: The case of monolayers and bilayers, Nano Lett. **11**, 1804 (2011).
[57] Z. Chen, P. Zhan, Z. Wang, J. Zhang, W. Zhang, N. Ming, C. T. Chan, and P. Sheng, Two-and three-dimensional ordered structures of hollow silver spheres prepared by colloidal crystal templating, Adv. Mater. **16**, 417 (2004).
[58] Z. Wang, T. Zhang, B. K. Park, W. I. Lee, and D. J. Hwang, Minimal contact formation between hollow glass microparticles toward low-density and thermally insulating composite materials, J. Mater. Sci. **52**, 6726 (2017).
[59] J. L. Rose, *Ultrasonic waves in solid media* (Cambridge University Press, Cambridge, 2004).